Author Manuscript

Author Manuscript

Author Manuscript

Author Manuscript

HHS Public Access

Author manuscript

IEEE J Multiscale Multiphys Comput Tech. Author manuscript; available in PMC 2018 May 01.

Published in final edited form as:

IEEE J Multiscale Multiphys Comput Tech. 2018 ; 3: 3–15. doi:10.1109/JMMCT.2018.2802420.

An FMM-FFT Accelerated SIE Simulator for Analyzing EM Wave Propagation in Mine Environments Loaded With Conductors

Abdulkadir C. Yucel,
Department of Electrical Engineering and Computer Science, University of Michigan, Ann Arbor, MI 48109 USA. He is now with the School of Electrical and Electronic Engineering, Nanyang Technological University, Singapore 639798

Weitian Sheng,
Department of Electrical Engineering and Computer Science, University of Michigan, Ann Arbor, MI 48109 USA

Chenming Zhou [Member, IEEE],
Office of Mine Safety and Health Research, National Institute for Occupational Safety and Health, Pittsburgh, PA 15236 USA

Yang Liu [Member, IEEE],
Department of Electrical Engineering and Computer Science, University of Michigan, Ann Arbor, MI 48109 USA

Hakan Bagci [Senior Member, IEEE], and
Computer, Electrical, and Mathematical Science and Engineering Division, King Abdullah University of Science and Technology, Thuwal 23955, Saudi Arabia

Eric Michielssen [Fellow, IEEE]
Department of Electrical Engineering and Computer Science, University of Michigan, Ann Arbor, MI 48109 USA

Abstract

A fast and memory efficient three-dimensional full-wave simulator for analyzing electromagnetic (EM) wave propagation in electrically large and realistic mine tunnels/galleries loaded with conductors is proposed. The simulator relies on Muller and combined field surface integral equations (SIEs) to account for scattering from mine walls and conductors, respectively. During the iterative solution of the system of SIEs, the simulator uses a fast multipole method-fast Fourier transform (FMM-FFT) scheme to reduce CPU and memory requirements. The memory requirement is further reduced by compressing large data structures via singular value and Tucker decompositions. The efficiency, accuracy, and real-world applicability of the simulator are demonstrated through characterization of EM wave propagation in electrically large mine tunnels/galleries loaded with conducting cables and mine carts.

Correspondence to: Abdulkadir C. Yucel.

Author Manuscript Author Manuscript Author Manuscript Author Manuscript

Index Terms

Electromagnetic (EM) simulator; EM wave propagation; fast multipole method–fast Fourier transform (FMM-FFT) technique; frequency domain analysis; integral equations; mine tunnels

I. Introduction

Reliable wireless communication, sensing, and tracking systems in underground mine environments are critically important to ensure workers' safety and productivity during routine operations and catastrophic events. As mandated by the MINER Act of 2006 [1], U.S. mine operators are required to install reliable and disaster-proof communication systems that support two-way post event communication and tracking functions. The development, operation, and reconfiguration of these systems, as well as the mitigation of possible electromagnetic (EM) compatibility and interference issues associated with their deployment, all benefit from EM simulation tools. These tools should be capable of analyzing EM wave propagation in mine tunnels and galleries that are loaded with conductors (e.g., lighting/power cables, mine carts, mining machinery, rails, ventilation systems), occupied by miners, and possibly obstructed by cave-in debris.

Present simulation techniques for analyzing EM wave propagation in mine environments are either approximate or full-wave in nature. Examples of approximate techniques include, but are not limited to, single/multimode waveguide models [2], [3], ray-tracing techniques [4]–[6], and cascaded-impedance methods [7]. The equivalence of the ray tracing and modal methods have been discussed in [8]. For other approximate techniques, see [9] and references therein. The above-referenced techniques typically only apply to EM characterization in restricted frequency bands and do not readily account for the presence of conductors and miners, wall roughness (especially when comparable to the wavelength), or unstructured debris. Full-wave techniques for analyzing EM wave propagation in mine environments include finite difference time domain [10]–[14] and surface integral equation (SIE) methods [15]. In principle, these techniques permit faithful modeling of EM wave propagation in real-world mine environments. However, in practice, due to their high-computational requirements, their applicability is limited to the study of EM wave propagation in electrically small or moderately sized tunnels even when they are implemented on graphics processing units [10].

This paper presents a fast, full-wave, CPU, and memory-efficient three-dimensional (3-D) SIE technique for analyzing EM wave propagation in electrically large and realistically loaded mine environments. The technique leverages Muller and combined field SIEs to model scattering from mine walls and perfect electrically conducting (PEC) objects residing inside mine tunnels and galleries. The naive iterative solution of such SIEs requires $O(N^2)$ CPU and memory resources. Here N is the number of basis functions used to discretize current densities on the mine walls and PEC objects. These requirements are prohibitive even when characterizing moderately sized tunnels and galleries. Therefore, the proposed simulator leverages a fast multipole method-fast Fourier transform (FMM-FFT) acceleration scheme [16] with $O(N^{4/3}\log^{2/3}N)$ CPU and memory resources [17] when applied to mine

Author Manuscript Author Manuscript Author Manuscript Author Manuscript

environments of arbitrary layout, and $O(N \log N)$ resources when applied to straight long tunnels or mine galleries populated with dense posts [16]. When applied to the analysis of EM propagation in mine environments, FMM-FFT accelerated SIE simulators tend to be memory—as opposed to CPU—limited. The simulators' memory requirements derive from the requirement to store the following:

1. near-field interaction matrices;
2. matrices that characterize far-field signatures of basis functions;
3. tensors that hold FFT'ed translation operators on a structured grid.

The proposed simulator compresses the first two and third data structures via singular value decomposition (SVD) and its higher-dimensional counterpart, Tucker decomposition [18], respectively. These compression schemes enable the application of the FMM-FFT accelerated SIE simulator to the analysis of EM wave propagation in much larger and complex mine environments. The paper's contributions are two-fold. First, it describes the first-ever application of a fast SIE simulator to the characterization of EM wave propagation in electrically large and realistically loaded mine environments. Second, it proposes a scheme, which compresses all large data structures of the FMM-FFT accelerated SIE simulator, to reduce its memory requirement and enable its application to larger scale problems on memory-bound computer clusters. The accuracy, efficiency, and applicability of the proposed simulator is demonstrated via the analysis of EM wave propagation in a 600 m-long arched tunnel loaded with conductors, a mine gallery consisting of eight rectangular tunnels, and a rectangular tunnel with rough walls.

II. Formulation

This section details the Muller and combined field SIEs and their numerical solution via the method of moments (MoM). It also elucidates the proposed SVD and Tucker-enhanced FMMFFT acceleration scheme.

A. SIEs and their Discretization

Let S_d denote the walls of a closed mine tunnel or gallery, which is surrounded by unbounded lossy ore with permittivity ε_1 and permeability μ_1 (medium 1). The tunnel or gallery is assumed to be filled by air with permittivity ε_0 and permeability μ_0 (medium 0) [see Fig. 1(a)]. (Note: the scheme detailed below can be trivially modified for tunnels and galleries filled by dust with permittivity different from ε_0.) Let S_p represent the arbitrarily shaped open or closed surfaces of PEC objects (e.g., mine carts, cables, or other equipment) residing inside S_d. S_d and S_p are excited by the incident EM field $\{\mathbf{E}^i(\mathbf{r}), \mathbf{H}^i(\mathbf{r})\}$ that is generated by a transmitter's electric current density $\mathbf{J}^i(\mathbf{r})$ (e.g., an electric dipole) residing within S_d [see Fig. 1(a)]. The interaction of $\{\mathbf{E}^i(\mathbf{r}), \mathbf{H}^i(\mathbf{r})\}$ with S_d and S_p gives rise to electric and magnetic current densities, $\mathbf{J}_d(\mathbf{r})$ and $\mathbf{M}_d(\mathbf{r})$ on S_d and electric current densities, $\mathbf{J}_p(\mathbf{r})$ on S_p.

To compute $\mathbf{J}_d(\mathbf{r})$, $\mathbf{M}_d(\mathbf{r})$, and $\mathbf{J}_p(\mathbf{r})$, the surface equivalence principle is invoked to construct the exterior and interior problems illustrated in Fig. 1(b) and 1(c). In the exterior problem [see Fig. 1(b)], $\mathbf{J}_d(\mathbf{r})$ and $\mathbf{M}_d(\mathbf{r})$ radiate in medium 1 and generate total and zero

Author Manuscript Author Manuscript Author Manuscript Author Manuscript

electric and magnetic fields exterior and interior to S_d, respectively. Imposing boundary conditions on the tangential components of electric and magnetic fields on S_d yields the following exterior electric field integral equation (EFIE) and magnetic field integral equation (MFIE):

$$0 = (0.5\mathbf{M}_d(\mathbf{r}) - \hat{\mathbf{n}}_d \times \mathfrak{R}_1[\mathbf{M}_d(\mathbf{r})]) + \mathbf{n}_d \times \mathfrak{F}_1[\mathbf{J}_d(\mathbf{r})] \quad (1)$$

$$0 = \hat{\mathbf{n}}_d \times \mathfrak{F}_1[\mathbf{M}_d(\mathbf{r})]/\eta_1^2 + (-0.5\mathbf{J}_d(\mathbf{r}) + \hat{\mathbf{n}}_d \times \mathfrak{R}_1[\mathbf{J}_d(\mathbf{r})]) \quad (2)$$

$\mathbf{r} \in S_d$. Here, $\hat{\mathbf{n}}_d$ is the outward normal to S_d, $\eta_a = (\mu_a/\varepsilon_a)^{0.5}$ with $a \in \{0, 1\}$ is the wave impedance, and the source-field operators $\mathfrak{F}_a[\cdot]$ and $\mathfrak{R}_a[\cdot]$ are

$$\mathfrak{F}_a[\mathbf{X}(\mathbf{r})] = -j\omega\mu_a \int_S \left(\bar{\mathbf{I}} + \frac{\nabla\nabla'}{k_a^2}\right) \cdot \mathbf{X}(\mathbf{r}') G_a(\mathbf{r}, \mathbf{r}')\, d\mathbf{r}' \quad (3)$$

$$\mathfrak{R}_a[\mathbf{X}(\mathbf{r})] = \nabla \times \int_S \mathbf{X}(\mathbf{r}') G_a(\mathbf{r}, \mathbf{r}')\, d\mathbf{r}' \quad (4)$$

where the integral in (4) is evaluated in the principal value sense. Here $G_a(\mathbf{r}, \mathbf{r}') = \exp(-jk_a|\mathbf{r} - \mathbf{r}'|)/(4\pi|\mathbf{r} - \mathbf{r}'|)$ is the scalar Green's function, $k_a = \omega(\mu_a\varepsilon_a)^{0.5}$, $\omega = 2\pi f$, f is the frequency, and $\mathbf{r}$ and $\mathbf{r}'$ denote observation and source locations on support S, respectively.

In the interior problem [see Fig. 1(c)], $-\mathbf{J}_d(\mathbf{r})$ and $-\mathbf{M}_d(\mathbf{r})$ radiate alongside $\mathbf{J}^i(\mathbf{r})$ and $\mathbf{J}_p(\mathbf{r})$ in air and generate total and zero electric and magnetic fields interior and exterior to S_d, respectively. Imposing boundary conditions for tangential electric and magnetic fields on S_d and S_p yields the following interior EFIE and MFIE for S_d and interior EFIE and MFIE for S_p:

$$\hat{\mathbf{n}}_d \times \mathbf{E}^i(\mathbf{r}) = -(0.5\mathbf{M}_d(\mathbf{r}) + \hat{\mathbf{n}}_d \times \mathfrak{R}_0[\mathbf{M}_d(\mathbf{r})]) + \hat{\mathbf{n}}_d \times \mathfrak{F}_0[\mathbf{J}_d(\mathbf{r})] - \hat{\mathbf{n}}_d \times \mathfrak{F}_0[\mathbf{J}_p(\mathbf{r})], \quad \mathbf{r} \in S_d \quad (5)$$

$$\hat{\mathbf{n}}_d \times \mathbf{H}^i(\mathbf{r}) = \hat{\mathbf{n}}_d \times \mathfrak{F}_0[\mathbf{M}_d(\mathbf{r})]/\eta_0^2 + (0.5\mathbf{J}_d(\mathbf{r}) + \hat{\mathbf{n}}_d \times \mathfrak{R}_0[\mathbf{J}_d(\mathbf{r})]) - \mathbf{n}_d \times \mathfrak{R}_0[\mathbf{J}_p(\mathbf{r})], \quad \mathbf{r} \in S_d \quad (6)$$

Author Manuscript Author Manuscript Author Manuscript Author Manuscript

$$\hat{\mathbf{t}}_p \cdot \mathbf{E}^i(\mathbf{r}) = \hat{\mathbf{t}}_p \cdot (-\mathfrak{R}_0[\mathbf{M}_d(\mathbf{r})] + \mathfrak{F}_0[\mathbf{J}_d(\mathbf{r})] - \mathfrak{F}_0[\mathbf{J}_p(r)]), \quad \mathbf{r} \in S_p \quad (7)$$

$$\hat{\mathbf{n}}_p \times \eta_0 \mathbf{H}^i(\mathbf{r}) = \hat{\mathbf{n}}_p \times \mathfrak{F}_0[\mathbf{M}_d(\mathbf{r})]/\eta_0 + \hat{\mathbf{n}}_p \times \eta_0 \mathfrak{R}_0[\mathbf{J}_d(\mathbf{r})] + \eta_0 (0.5\mathbf{J}_p(\mathbf{r}) - \hat{\mathbf{n}}_p \times \mathfrak{R}_0[\mathbf{J}_p(\mathbf{r})]), \quad \mathbf{r} \in S_p. \quad (8)$$

Here $\hat{\mathbf{n}}_p$ and $\hat{\mathbf{t}}_p$ are the outward pointing unit normal and arbitrary unit vector tangential to S_p, respectively. Exterior and interior EFIEs for S_d in (1) and (5) can be linearly combined after multiplying them by α_1 and α_0, respectively, as

$$\hat{\mathbf{n}}_d \times \alpha_0 \mathbf{E}^i(\mathbf{r}) = 0.5(\alpha_1 - \alpha_0)\mathbf{M}_d(\mathbf{r}) - \hat{\mathbf{n}}_d \times (\alpha_1 \mathfrak{R}_1[\mathbf{M}_d(\mathbf{r})] + \alpha_0 \mathfrak{R}_0[\mathbf{M}_d(\mathbf{r})]) + \hat{\mathbf{n}}_d \times (\alpha_1 \mathfrak{F}_1[\mathbf{J}_d(\mathbf{r})] + \alpha_0 \mathfrak{F}_0[\mathbf{J}_d(\mathbf{r})]) - \hat{\mathbf{n}}_d \times \alpha_0 \mathfrak{F}_0[\mathbf{J}_p(\mathbf{r})]. \quad (9)$$

Similarly, exterior and interior MFIEs for S_d can be multiplied by β_1 and β_0, respectively, and combined as

$$\hat{\mathbf{n}}_d \times \beta_0 \mathbf{H}^i(\mathbf{r}) = \hat{\mathbf{n}}_d \times \left(\frac{\beta_1}{\eta_1^2} \mathfrak{F}_1[\mathbf{M}_d(\mathbf{r})] + \frac{\beta_0}{\eta_0^2} \mathfrak{F}_0[\mathbf{M}_d(\mathbf{r})] \right) + 0.5(\beta_0 - \beta_1)\mathbf{J}_d(\mathbf{r}) + \hat{\mathbf{n}}_d \times (\beta_1 \mathfrak{R}_1[\mathbf{J}_d(\mathbf{r})] + \beta_0 \mathfrak{R}_0[\mathbf{J}_d(\mathbf{r})]) - \hat{\mathbf{n}}_d \times \beta_0 \mathfrak{R}_0[\mathbf{J}_p(\mathbf{r})]. \quad (10)$$

Finally, linearly combining the α_p times interior EFIE and $(1 - \alpha_p)$ times interior MFIE for S_p yields

Author Manuscript Author Manuscript Author Manuscript Author Manuscript

$$\begin{aligned}&\hat{\mathbf{t}}_p \cdot \alpha_p \mathbf{E}^i(\mathbf{r}) + \hat{\mathbf{n}}_p \times \eta_0 (1-\alpha_p)\, \mathbf{H}^i(\mathbf{r}) \\ &= (-\hat{\mathbf{t}}_p \cdot \alpha_p \mathfrak{R}_0 [\mathbf{M}_d(\mathbf{r})] + \hat{\mathbf{n}}_p \times (1-\alpha_p)/\eta_0 \mathfrak{T}_0 [\mathbf{M}_d(\mathbf{r})]) \\ &+ (\hat{\mathbf{t}}_p \cdot \alpha_p \mathfrak{T}_0 [\mathbf{J}_d(\mathbf{r})] + \hat{\mathbf{n}}_p \times \eta_0 (1-\alpha_p)\, \mathfrak{R}_0 [\mathbf{J}_d(\mathbf{r})]) \\ &+ (-\hat{\mathbf{t}}_p \cdot \alpha_p \mathfrak{T}_0 [\mathbf{J}_p(\mathbf{r})] + \eta_0 (1-\alpha_p) \cdot (0.5\mathbf{J}_p(\mathbf{r}) - \hat{\mathbf{n}}_p \times \mathfrak{R}_0 [\mathbf{J}_p(\mathbf{r})]))\,.\end{aligned} \tag{11}$$

Equations (9)–(11) with $\alpha_1 = \varepsilon_1$, $\alpha_0 = -\varepsilon_0$, $\beta_1 = \mu_1$, $\beta_0 = -\mu_0$, and $0 \le \alpha_p \le 1$ are known as Muller-combined field SIE formulation [19] and can be solved simultaneously for $\mathbf{M}_d(\mathbf{r})$, $\mathbf{J}_d(\mathbf{r})$, and $\mathbf{J}_p(\mathbf{r})$ via the MoM. (Note: In this study, α_p is set to 0.2 and 1 for closed and open PEC surfaces, respectively.) To this end, $\mathbf{M}_d(\mathbf{r})$, $\mathbf{J}_d(\mathbf{r})$, and $\mathbf{J}_p(\mathbf{r})$ are approximated in terms of Rao–Wilton–Glisson (RWG) basis functions $\mathbf{f}_n(\mathbf{r})$ [20] as

$$\mathbf{M}_d(\mathbf{r}) = \sum_{n=1}^{N_d} I_n \mathbf{f}_n(\mathbf{r}) \quad \mathbf{J}_d(\mathbf{r}) = \sum_{n=N_d+1}^{2N_d} I_n \mathbf{f}_n(\mathbf{r}) \tag{12}$$

$$\mathbf{J}_p(\mathbf{r}) = \sum_{n=2N_d+1}^{2N_d+N_p} I_n \mathbf{f}_n(\mathbf{r}) \tag{13}$$

where I_n, $n = 1, \ldots, 2N_d + N_p$, are unknown expansion co-efficients. Substituting (12) and (13) into (9)–(11) and applying Galerkin testing to the resulting equations with $\mathbf{f}_m(\mathbf{r})$, $m = 1, \ldots, 2N_d + N_p$, yields the linear system of equations of dimension $N = 2N_d + N_p$

$$\bar{\mathbf{Z}}\mathbf{I} = \mathbf{V} \tag{14}$$

where $\bar{\mathbf{Z}}$ is the MoM matrix, and $\mathbf{I}$ and $\mathbf{V}$ are vectors of unknown expansion coefficients and tested incident EM fields, respectively. The entries of $\mathbf{I}$, I_n, $n = 1, \ldots, N$, as well as those of $\bar{\mathbf{Z}}$ and $\mathbf{V}$ are provided in Appendix I.

When analyzing electrically large mine tunnels and galleries loaded with conductors that require large N, the solution of the matrix system in (14) cannot be obtained using classical algebraic solvers. To mitigate the computational and memory requirements of the iterative solution of (14), we deploy the SVD and Tucker enhanced FMM-FFT scheme described next.

B. SVD and Tucker Enhanced FMM-FFT Algorithm

1) FMM-FFT Algorithm—The FMM-FFT scheme introduces a hypothetical box enclosing the mesh of S_d (and hence S_p). This large box is split into N_x, N_y, and N_z smaller boxes

Author Manuscript Author Manuscript Author Manuscript Author Manuscript

along the x, y, and z directions [see Fig. 2]. The resulting boxes are denoted by $B_{\mathbf{u}}$ with indices $\mathbf{u} = (u_x, u_y, u_z)$, $u_x = 1, \ldots, N_x$, $u_y = 1, \ldots, N_y$, $u_z = 1, \ldots, N_z$, and centered at $\mathbf{r}_{\mathbf{u}}$ that coincide with the points of a uniform 3-D grid [see Fig. 2]. All boxes that contain triangle pairs of source/testing basis functions, $\mathbf{f}_n(\mathbf{r})/\mathbf{f}_m(\mathbf{r})$, are termed "groups" and enclosed by a sphere of radius R^s. Two groups $B_{\mathbf{u}}$ and $B_{\mathbf{u}'}$ constitute a near-field pair if the distance between their centers $R_{\mathbf{u}'\mathbf{u}} = |\mathbf{R}_{\mathbf{u}'\mathbf{u}}| = |\mathbf{r}_{\mathbf{u}'} - \mathbf{r}_{\mathbf{u}}|$ is smaller than a prescribed threshold, i.e., $R_{\mathbf{u}'\mathbf{u}} < \kappa R^s$; otherwise, they form a far-field pair [see Fig. 2].

Interactions between basis functions in the same group and near-field pairs are directly computed via (27)–(35) (in Appendix I) and stored, resulting in the first large data structure mentioned in the introduction. A large portion of this data structure is pertinent to interactions between basis functions in near-field pairs and compressed by SVD, as elucidated in the following section. The contributions of self and near-field interactions to the result of each matrix-vector multiplication required by the iterative solution of (14) are directly computed. The interactions between basis functions in far-field pairs are computed by the FMM-FFT algorithm. To this end, first, the far-field patterns of source basis functions $\mathbf{P}^+(\hat{\mathbf{k}}_a^{pq}, \mathbf{f}_n)$ with

$$\mathbf{P}^{\pm}(\hat{\mathbf{k}}_a^{pq}, \mathbf{c}) = \int_{S_c} \exp(\pm jk_a \hat{\mathbf{k}}_a^{pq} \cdot (\mathbf{r} - \mathbf{r}_{\mathbf{u}}))(\bar{\mathbf{I}} - \hat{\mathbf{k}}_a^{pq}\hat{\mathbf{k}}_a^{pq}) \cdot \mathbf{c}(\mathbf{r}) d\mathbf{r} \quad (15)$$

are computed and stored for all directions $\hat{\mathbf{k}}_a^{pq} = (\sin\theta^p \cos\phi^q, \sin\theta^p \sin\phi^q, \cos\theta^p)$, $p = 1, \ldots, K_a + 1$, $q = 1, \ldots, 2K_a + 1$. Here, θ^p are the inverse cosine of abscissas of $(K_a + 1)^{\text{th}}$–order Gauss–Legendre quadrature rule, $\phi^q = q2\pi/(2K_a + 1)$, $K_a = 2k_a R^s + 1.8(\log_{10}(1/\gamma_1))^{2/3}(2k_a R^s)^{1/3}$ is the number of multipoles for medium $a = \{0, 1\}$, γ_1 is the number of desired accurate digits in the FMM approximation [21], S_c is the support of $\mathbf{c}(\mathbf{r})$, and $\mathbf{u}$ corresponds to the box containing $\mathbf{c}(\mathbf{r})$. Since $\bar{\mathbf{I}}$ is unit dyad and $\bar{\mathbf{I}} - \hat{\mathbf{k}}_a^{pq}\hat{\mathbf{k}}_a^{pq} = \hat{\theta}\theta + \hat{\phi}\hat{\phi}$, θ and ϕ components of far-field patterns are computed [21]. Note that only the far-field patterns of source basis functions discretizing $\mathbf{J}_d(\mathbf{r})$and $\mathbf{J}_p(\mathbf{r})$ are computed and stored for both media and only air (medium 0), respectively; the ones pertinent to $\mathbf{M}_d(\mathbf{r})$ can be directly obtained from those related to $\mathbf{J}_d(\mathbf{r})$ by invoking the duality and thereby are not stored. Similarly, the receiving patterns of testing functions used to test electric and magnetic fields on S_d, $\mathbf{P}^-(\hat{\mathbf{k}}_a^{pq}, \hat{\mathbf{n}}_d \times \mathbf{f}_m)$, and electric and magnetic fields on S_p, $\mathbf{P}^-(\hat{\mathbf{k}}_a^{pq}, \mathbf{f}_m)$ and $\mathbf{P}^-(\hat{\mathbf{k}}_a^{pq}, \hat{\mathbf{n}}_p \times \mathbf{f}_m)$, are computed and stored for both media and only air, respectively. These operations give rise to the second large data structure alluded to in Section I, which is compressed by SVD, as explained in the following section. During matrix-vector multiplication, the far-fields of basis functions in each group are summed to construct all groups' outgoing far-field patterns for both media as

Author Manuscript Author Manuscript Author Manuscript Author Manuscript

$$\mathcal{F}_{\mathbf{u}}(\hat{\mathbf{k}}_a^{pq}) = \sum_{n \in B_{\mathbf{u}}} \mathbf{P}^{+}(\hat{\mathbf{k}}_a^{pq}, \mathbf{f}_n)\alpha_a c I_n \quad (16)$$

$p = 1, \ldots, K_a + 1$, $q = 1, \ldots, 2K_a + 1$, $a \in \{0, 1\}$. Here c is -1 for far-field patterns of basis functions used to discretize $\mathbf{J}_p(\mathbf{r})$ and 1 otherwise. (Note: far-field patterns of basis functions discretizing $\mathbf{J}_p(\mathbf{r})$ are not computed/stored for medium 1 and not included in summation in (16) for $a = 1$.) Next, for each $\hat{\mathbf{k}}_a^{pq}$, these far-field patterns $\mathcal{F}_{\mathbf{u}}(\hat{\mathbf{k}}_a^{pq})$ are convolved via FFT with the translation tensor $\mathcal{T}^{\sim}_{\mathbf{u}'-\mathbf{u}}(\hat{\mathbf{k}}_a^{pq})$ to obtain all groups' incoming plane wave spectra $\mathcal{G}_{\mathbf{u}'}(\hat{\mathbf{k}}_a^{pq})$ as

$$\mathcal{G}_{\mathbf{u}'}(\hat{\mathbf{k}}_a^{pq}) = \Psi^{-1}(\mathcal{T}_{\mathbf{u}'-\mathbf{u}}(\hat{\mathbf{k}}_a^{pq})\Psi(\mathcal{F}_{\mathbf{u}}(\hat{\mathbf{k}}_a^{pq}))). \quad (17)$$

Here Ψ is the FFT operator, $\mathcal{T}_{\mathbf{u}'-\mathbf{u}}(\hat{\mathbf{k}}_a^{pq}) = \Psi(\mathcal{T}^{\sim}_{\mathbf{u}'-\mathbf{u}}(\hat{\mathbf{k}}_a^{pq}))$ is the tensor that stores FFT'ed translation operator values and

$$\mathcal{T}^{\sim}_{\mathbf{u}'-\mathbf{u}}(\hat{\mathbf{k}}_a^{pq}) = \frac{k_a^2 \eta_a}{16\pi^2} \sum_{l=1}^{K_a} (-j)^l (2l+1) h_l^{(2)}(k_a R_{\mathbf{u}'\mathbf{u}}) \Phi_l(\hat{\mathbf{R}}_{\mathbf{u}'\mathbf{u}} \cdot \hat{\mathbf{k}}_a^{pq}). \quad (18)$$

where $\hat{\mathbf{R}}_{\mathbf{u}'\mathbf{u}} = \mathbf{R}_{\mathbf{u}'\mathbf{u}}/R_{\mathbf{u}'\mathbf{u}}$, $\Phi_l(\cdot)$ is the Legendre polynomial of degree l and $h_l^{(2)}$ denotes the spherical Hankel function of the second kind. All $\mathcal{T}_{\mathbf{u}'-\mathbf{u}}(\hat{\mathbf{k}}_a^{pq})$ computed and stored for all directions constitute the third large data structure mentioned in Section I and can be compressed via Tucker decomposition [18], as explained in the following section.

In practice, the circular convolution in (17) for each $\hat{\mathbf{k}}_a^{pq}$ is performed as follows. First, $\mathcal{T}_{\mathbf{u}'-\mathbf{u}}(\hat{\mathbf{k}}_a^{pq})$ is computed by Fourier transforming $\mathcal{T}^{\sim}_{\mathbf{u}'-\mathbf{u}}(\hat{\mathbf{k}}_a^{pq})$ with indices $u'_x = -N_x + 1, \ldots, N_x$, $u'_y = -N_y + 1, \ldots, N_y$, $u'_z = -N_z + 1, \ldots, N_z$, $(u'_x, u'_y, u'_z \neq 0)$, and $\mathbf{u} = (1, 1, 1)$. Second, $\mathcal{T}_{\mathbf{u}'-\mathbf{u}}(\hat{\mathbf{k}}_a^{pq})$ is multiplied with the Fourier transform of $\mathcal{F}_{\mathbf{u}}(\hat{\mathbf{k}}_a^{pq})$ with indices $u_x = 1, \ldots, N_x$, $u_y = 1, \ldots, N_y$, $u_z = 1, \ldots, N_z$, after the dimensions of $\mathcal{F}_{\mathbf{u}}(\hat{\mathbf{k}}_a^{pq})$ are increased to $(2N_x - 1) \times (2N_y - 1) \times (2N_z - 1)$ by zero padding. After computing all $\mathcal{G}_{\mathbf{u}'}(\hat{\mathbf{k}}_a^{pq})$, those are projected onto the testing basis functions and far-field contributions to the matrix-vector multiplication in (14) are computed by summing over all directions with quadrature weights w_a^{pq} as

Author Manuscript Author Manuscript Author Manuscript Author Manuscript

$$\sum_{a=0}^{1}\sum_{p=1}^{K_a+1}\sum_{q=1}^{2K_a+1} w_a^{pq}\mathbf{P}^{-}(\hat{\mathbf{k}}_a^{pq},\hat{\mathbf{n}}_d\times\mathbf{f}_m)\cdot\mathcal{G}_{\mathbf{u}'}(\hat{\mathbf{k}}_a^{pq}),\quad 1\le m\le N_d \tag{19}$$

$$\sum_{a=0}^{1}\sum_{p=1}^{K_a+1}\sum_{q=1}^{2K_a+1} w_a^{pq}\left(\mathbf{P}^{-}(\hat{\mathbf{k}}_a^{pq},\hat{\mathbf{n}}_d\times\mathbf{f}_m)\times\hat{\mathbf{k}}_a^{pq}\right)\cdot\mathcal{G}_{\mathbf{u}'}(\hat{\mathbf{k}}_a^{pq})(\beta_a/\alpha_a),\quad N_d+1\le m\le 2N_d \tag{20}$$

$$\sum_{p=1}^{K_0+1}\sum_{q=1}^{2K_0+1} w_0^{pq}/\alpha_0\left(\alpha_p\mathbf{P}^{-}(\hat{\mathbf{k}}_0^{pq},\mathbf{f}_m)-(1-\alpha_p)\mathbf{P}^{-}(\hat{\mathbf{k}}_0^{pq},\hat{\mathbf{n}}_p\times\mathbf{f}_m)\times\hat{\mathbf{k}}_0^{pq}\right)\cdot\mathcal{G}_{\mathbf{u}'}(\hat{\mathbf{k}}_0^{pq}),\quad 2N_d$$

$$+1\le m\le N. \tag{21}$$

To execute the FMM-FFT algorithm on high-performance parallel computers for characterizing large-scale mine tunnels/galleries loaded with conductors, a hybrid spatial/angular parallelization strategy, which utilizes hybrid message passing interface/open multiprocessing (MPI/OpenMP) standards, is deployed. This parallelization strategy, described in Appendix II, uniformly partitions the memory and computational loads along angular dimension (i.e., plane-wave directions) and spatial dimension (i.e., groups) among processors. Such parallelization strategy introduces two additional processor-to-processor communications compared to the spatial partitioning strategy in [22]. These additional communications require negligible time when nonblocking MPI operations are used. On the other hand, the hybrid spatial/angular parallelization strategy permits scalable workload partitioning of compression of far-field patterns, while the spatial parallelization strategy in [22] does not.

2) SVD and Tucker Decomposition Enhancements—To reduce the memory requirement of the SIE simulator leveraging FMM-FFT algorithm, large data structures storing the near-field interactions, far-field (and receiving) patterns of basis functions, and FFT'ed translation operator tensors are compressed viaSVD and its higher-dimensional counterpart Tucker decomposition.

Compression of near-field interaction matrices: Assume that the near-field interactions between N_s source basis functions in a group $B_{\mathbf{u}}$ (e.g., $\mathbf{u}$ = (1, 1, 1) in Fig. 2) and N_t testing basis functions in a group $B_{\mathbf{u}'}$ (e.g., $\mathbf{u}'$ = (2, 1, 1) in Fig. 2) are stored in a matrix $\bar{\mathbf{Q}}$ with dimensions $N_t \times N_s$, which is a rank deficient block of MoM matrix with entries $\bar{\mathbf{Z}}_{mn}$, $m \in B_{\mathbf{u}'}$, $n \in B_{\mathbf{u}}$, and can be compressed via truncated SVD (TrSVD(·)) as

Author Manuscript Author Manuscript Author Manuscript Author Manuscript

$$\bar{\mathbf{Q}} \approx \mathrm{TrSVD}(\bar{\mathbf{Q}}) = \bar{\mathbf{U}}\bar{\boldsymbol{\Sigma}}\bar{\mathbf{V}}^{*} \quad (22)$$

where * stands for conjugate transpose, $\bar{\mathbf{U}}$ and $\bar{\mathbf{V}}$ are truncated unitary matrices with dimensions $N_t \times r$ and $N_s \times r$, respectively, and $\bar{\boldsymbol{\Sigma}}$ is the diagonal matrix with descending r singular values of $\bar{\mathbf{Q}}$, δ_i, $i = 1, \ldots, r$, which are greater than a prescribe tolerance γ_2 times the value of first singular value, i.e., $\delta_i \geq \gamma_2 \delta_1$, $i = 1, \ldots, r$. During the setup stage, truncated SVD compression is applied to all MoM matrix blocks that stores the near-field interactions between groups, but not applied to full rank blocks pertinent to self-interactions of groups. During the iterative solution of (14), the reduced representations in (22) are directly used without restoring the full block $\bar{\mathbf{Q}}$ to compute the contributions of near-field interactions to the matrix vector multiplication.

Compression of matrices holding far-field patterns: Assume that one component (θ or ϕ) of far-field (or receiving) pattern of a basis function for a medium $a \in \{0, 1\}$ is stored in a matrix $\bar{\mathbf{W}}$ with dimensions $(K_a + 1) \times (2K_a + 1)$, which tabulates the farfield samples along elevation and azimuthal directions through its rows and columns, respectively. Given the prescribed tolerance γ_3, $\bar{\mathbf{W}}$ can be approximated by its truncated SVD as

$$\bar{\mathbf{W}} \approx \mathrm{TrSVD}(\bar{\mathbf{W}}). \quad (23)$$

This operation is applied to θ and ϕ components of all basis functions' far-field and receiving patterns for both media. The resulting truncated unitary matrices and singular values obtained and stored during setup stage are used to restore the far-field and receiving patterns one-by-one during the iterative solution of (14).

Compression of FFT'ed translation operator tensors: The tensor storing the FFT'ed translation operator samples for each $\hat{\mathbf{k}}_a^{pq}$, $\mathcal{T}_{\mathbf{u}'-\mathbf{u}}$, has dimensions $D_1 \times D_2 \times D_3 = (2N_x - 1) \times (2N_y - 1) \times (2N_z - 1)$ and can be compressed via Tucker decomposition as [23]

$$\mathcal{T}_{\mathbf{u}'-\mathbf{u}} \approx \mathcal{X} \times_1 \bar{\mathbf{U}}_1 \times_2 \bar{\mathbf{U}}_2 \times_3 \bar{\mathbf{U}}_3 \quad (24)$$

where $\mathcal{X}$ is the core tensor with dimensions $r_1 \times r_2 \times r_3$, $\bar{\mathbf{U}}_i$, $i = 1, \ldots, 3$, denote the factor matrices with dimensions $D_i \times r_i$, $i = 1, \ldots, 3$, and $\times_i$, $i = 1, \ldots, 3$, stands for the i–mode matrix product of a tensor, which can be performed as explained in [24]. The core tensor and factor matrices are obtained via the following procedure:

1. The unfolding matrices of $\mathcal{T}_{\mathbf{u}'-\mathbf{u}}$, $\bar{\mathbf{T}}_i$, $i = 1, \ldots, 3$, are formed. (Note: An example of forming unfolding matrices of a tensor is given in [24, eq. 2.1]).

Author Manuscript Author Manuscript Author Manuscript Author Manuscript

2. Given the prescribed tolerance $\gamma_4/\sqrt{3}$, the truncated SVDs of unfolding matrices, $\mathrm{TrSVD}(\overline{\mathbf{T}}_i) = \overline{\mathbf{U}}_i\overline{\mathbf{\Sigma}}_i\overline{\mathbf{V}}_i^*$, $i = 1, \ldots, 3$, are obtained. The resulting truncated unitary matrices $\tilde{\mathbf{U}}_i$, $i = 1, \ldots, 3$, are the factor matrices of (24).

3. The core tensor can be obtained via

$$\mathcal{X} = \mathcal{T}_{\mathbf{u}'-\mathbf{u}} \times_1 \overline{\mathbf{U}}_1^* \times_2 \overline{\mathbf{U}}_2^* \times_3 \overline{\mathbf{U}}_3^*. \quad (25)$$

The core tensors and factor matrices of FFT'ed translation operator tensors for all $\hat{\mathbf{k}}_a^{pq}$ directions are obtained during the setup stage and used to restore $\mathcal{T}_{\mathbf{u}'-\mathbf{u}}$ one $\mathbf{k}_a^{pq}$ at a time during the iterative solution stage.

III. Numerical Results and Discussion

This section presents numerical examples that demonstrate the accuracy, efficiency, and applicability of the proposed FMM-FFT- SIE simulator. In all examples below, the FMM box size is half of the wavelength in ore, FMM accuracy is three digits ($\gamma_1 = 3$), matrix system (14) is solved by a transpose-free quasiminimal residual iterative solver [25] with a residual error tolerance of 10^{-6}, which uses a right diagonal preconditioner, and tolerances γ_2, γ_3, and γ_4 for compressing matrices and tensors are 10^{-3}, 10^{-4}, and 10^{-6}, respectively. Furthermore, tunnels and galleries are surrounded by ore with permittivity $\varepsilon_1 = \varepsilon_0\,(\varepsilon_{r,1} - j\sigma_1/\omega\varepsilon_0)$ and permeability $\mu_1 = \mu_0$; $\varepsilon_{r,1}$and σ_1 are the relative permittivity and conductivity of the ore, respectively. All simulations are performed on a cluster of dual hexacore X5650 Intel processors with 64 GB RAM, launching one MPI process on each processor and distributing the computational load assigned to each processor among its 16 cores via OpenMP. The CPU and memory requirements of the proposed solver for all numerical examples are tabulated in Table I.

A. Arched Tunnel

First, the proposed simulator is used to analyze EM wave propagation in an arched tunnel surrounded by ore with $\varepsilon_{r,1} = 8.9$ and $\sigma_1 = 0.15$ S/m [see Fig. 3(a)]. A transmitting electrically small electric dipole with unit moment is positioned at (0.915, 50, 1.22) m and power densities are computed on lines inside the tunnel. Three different scenarios are considered: an empty tunnel, a tunnel loaded with mine carts, and a tunnel loaded with conducting strips that model a transmission line.

1) Empty Tunnel—A 600 m-long tunnel is excited by either a *z*– (vertically) or *x*– (horizontally) oriented dipole operated at 455 MHz or 915 MHz (4 cases) [see Fig. 3(a)]. At the lower and higher frequencies, the current densities on the tunnel walls are discretized using $N = 15, 153, 996$ and $N = 58, 510, 782$ RWG basis functions, respectively. Power densities computed on the line connecting (0.915, 51, 1.22) m and (0.915, 600, 1.22) m are compared with measured data [8], [26] following normalization to account for uncertainties/ differences in the excitation mechanism [see Fig. 3(b)–(e)]. Computed and measured power densities are in good agreement, thereby validating the accuracy of the simulator. The

Author Manuscript Author Manuscript Author Manuscript Author Manuscript

dynamic range of both the simulator and measurements is approximately 100 dB and reflected in Fig. 3(b), 3(c), and 3(e). The magnitude of the electric current density on the tunnel walls computed for each orientation of the transmitting dipole and frequency is shown in Fig. 3(f)–(i). The electric current density decays in accordance with the power density along the tunnel. It can be seen from Table I that the proposed compression schemes reduce the memory requirements of the simulator by factors of 2 for 455 MHz and 1.8 for 915 MHz. It should be noted here that the simulations at 915 MHz could not be executed on the current computer cluster using only the FMM-FFT acceleration. Memory requirement of the FMM-FFT accelerated simulator had to be reduced further using the compression schemes.

2) Tunnel Loaded With Mine Carts—A 200 m-long tunnel loaded with six PEC mine carts is excited by a z–directed electric dipole operated at 455 MHz [see Fig. 4(a)]. The mine carts are centered at (0.915, 80.25 + (j − 1) × 20, 0.55) m, j = 1, …, 6; their surfaces and wheels are modeled by truncated inverted pyramids and circular cylinders, respectively [see Fig. 4(a)]. The current densities on the tunnel walls and mine carts are discretized using N = 5, 433, 360 RWG basis functions. Power densities computed on the line connecting (0.915, 51, 1.22) m and (0.915, 200, 1.22) m are compared with those in the empty tunnel (obtained in scenario A) [see Fig. 4(b)]. The power density at y = 184 m (just after the sixth mine cart) is 9 dB below that observed in the empty tunnel. Oscillations in the power density graph in the loaded tunnel beyond y = 81 m, that is just after the first mine cart, result from reflections from subsequent carts, as evidenced by plots of the electric current density on tunnel walls displayed in Fig. 4(c). Again, the proposed compression schemes reduce the solver's memory requirement by a factor of two [see Table I].

3) Tunnel Loaded WITH Conducting Strips—A 650 m-long tunnel loaded with two PEC strips is excited by a z–directed electric dipole operated at 50 MHz [see Fig. 5(a)]. The PEC strips, which are 600 m long, infinitesimally thin, 4 cm wide, and separated by 0.3 m, model a transmission line placed near the lateral tunnel wall and are centered at (0.17, 345, 1.07)m and (0.17, 345, 1.37) m. The current densities on the tunnel walls and conducting strips are discretized using N = 442, 044 RWG basis functions and the simulation is performed without FMMFFT acceleration as the FMM-FFT algorithm is numerically unstable for low frequencies [21]. This is simply achieved by setting κ to a very large number and box size to one wavelength in ore, which ensures that all groups become near-field pairs and their interactions are compressed using SVD. Normalized power densities computed along two lines connecting point (0.915, 51, 1.22) m to (0.915, 645, 1.22) m (tunnel center), and point (0.17, 51, 1.22) m to (0.17, 645, 1.22) m (middle of strips) are shown in Fig. 5(b). A standing wave phenomenon can be observed at receiver points near to the wall at y = 650 m. The magnitude of the electric current densities induced on tunnel walls and conductor strips are shown in Fig. 5(c). The current densities induced on the strips conform to a bifilar mode [9], allowing the field to travel deep into the tunnel. The unloaded tunnel does not support any propagating modes.

B. Mine Gallery

Next, the proposed simulator is used to analyze EM wave propagation in a mine gallery formed by eight rectangular tunnels [see Fig. 6(a)], four of which extend along the x

Author Manuscript Author Manuscript Author Manuscript Author Manuscript

direction and intersect the remaining four extending along the y direction [see Fig. 6(a)]. The tunnels are surrounded by ore with $\varepsilon_{r,1} = 3$ and $\sigma_1 = 0.001$ S/m. The gallery is excited by an electric dipole with unit moment that is centered at (7.5, 15.91, 1.12)m), either z– (vertically) or y– (horizontally) oriented, and operated at either 455 or 915 MHz (four cases). The current densities on the walls are discretized using $N = 15, 766, 560$ and $N = 58, 794, 816$ RWG basis functions at the lower and higher frequencies, respectively. For both polarizations and frequencies, normalized power densities computed at receiver points along four lines in the x-directed tunnels connecting (8.5, y, 1.12) m to (81.5, y, 1.12) m with y set to 15.91, 32.73, 49.55, and 66.37 are shown in Fig. 6(b)–(e), The following observations are in order:

1. In tunnel 2, power densities at receivers with x–coordinates less than 15.91 m are always larger than those at receivers with x–coordinates exceeding 15.91 m [see Fig. 6(b)–(e)]. Slight or no decay is observed for receivers with x–coordinates lower than 15.91 m as direct coupling from the transmitter to these receiver points occurs through the low-loss ore.
2. Small or large spikes appear in the power density plots near receivers with x–coordinates 15.9, 32.7, 49.5, and 66.3 m in tunnels 3 and 4 [see Fig. 6(b)–(e)]. Note that these receivers reside at the intersections of tunnels 3 and 4 and tunnels 5, 6, 7, and 8; these spikes result from waves guided by tunnels 5, 6, 7, and 8.

The electric current densities on gallery walls computed for each frequency and polarization are shown in Fig. 6(f)–(i); these plots indirectly confirm the above power density observations. It can be seen in Table I that the proposed compression schemes reduce the memory requirements of the simulator by factors of 2 at 455 MHz and 1.6 at 915 MHz.

C. Rectangular Tunnel With Rough Walls

Finally, the proposed simulator is used to analyze EM wave propagation in a rectangular tunnel with rough walls, excited by a z– (vertically) oriented unit electric dipole positioned at (50.0, 0.925, 1.12) m and operated at 455 MHz [see Fig. 7(a)]. The tunnel is surrounded by ore with $\varepsilon_{r,1} = 3$ and $\sigma_1 = 0.001$ S/m. Tunnel walls have a random profile with 0.1 m root-mean-square height and 0.25 m correlation length [27]. The current densities on the tunnel walls are discretized using N=13, 580, 916 RWG basis functions. Results for the tunnel with rough walls are compared to those for the corresponding tunnel with smooth walls, and power densities are computed along a line connecting (51.0, 0.925, 1.12) m and (200, 0.925, 1.12) [see Fig. 7(b)]. The power density at $y = 175$ m for the tunnel with rough walls is 7.34 dB below that for the tunnel with smooth walls. Furthermore, the power densities computed by the proposed solver for the tunnel with smooth walls are compared to those obtained using the multimodal decomposition method of [3] in Fig. 7(b). Near-perfect agreement between the two results is observed, validating the accuracy of the proposed simulator one more time. In addition, the electric current densities computed on rough and smooth walls are shown in Fig. 7(c) and 7(d). Clearly, the decay of the current densities on tunnel walls for both cases conforms with the decay of the power densities along the tunnels. The proposed compression schemes reduce the solvers' memory requirements by a factor more than two [see Table I]. When the FMM-FFT accelerated simulator without the compression schemes is used for characterization of EM wave propagation in tunnels with

Author Manuscript Author Manuscript Author Manuscript Author Manuscript

rough and smooth walls, the simulations are completed in 4 h and 54 min and 4 h and 33 min, respectively. By comparing these simulation times with those in Table I, it can be concluded that for these examples, the compression schemes increase the simulation time by a factor around one-third.

IV. Conclusion

An FMM-FFT-SIE full-wave simulator is presented for characterizing EM wave propagation in electrically large and loaded mine environments. The full-wave simulator rapidly solves the Muller-combined field SIE system using a parallel FMM-FFT acceleration scheme. To reduce the memory requirements, the simulator employs SVDs to compress matrices characterizing near-field interactions and far-field (and receiving) patterns, and Tucker decompositions to compress tensors storing FFT'ed translation operator tensors. Numerical results demonstrate the accuracy, efficiency, and applicability of the proposed simulator. The proposed full-wave simulator is currently being used as a research tool for characterizing wireless channels and predicting radio coverage in underground mine tunnels and galleries. Wireless system manufacturers and network designers can potentially use the simulator to identify best node locations when deploying a wireless communication, tracking, or sensing system in underground mines, especially during an emergency when the mine is obstructed by debris from a cave-in. The coupling of the proposed simulator to fast and accurate uncertainty quantification frameworks [28]–[31] is being investigated for obtaining the statistics of observables due to uncertainty in mine geometry, configuration, and excitation [32].

Acknowledgments

This work was supported in part by the Alpha Foundation under Grant AFC215-54.

The findings and conclusions in this paper are those of authors and do not necessarily represent the views of the National Institute for Occupational Safety and Health.

References

1. *Mine Improvement and New Emergency Response Act of 2006 (MINER Act)*, ed: Pub. L. no. 108–236 (S 2803), 2006.
2. Emslie A, Lagace R, Strong P. Theory of the propagation of UHF radio waves in coal mine tunnels. IEEE Trans Antennas Propag. Mar; 1975 AP-23(2):192–205.
3. Sun Z, Akyildiz IF. Channel modeling and analysis for wireless networks in underground mines and road tunnels. IEEE Trans Commun. Jun; 2010 58(6):1758–1768.
4. Mahmoud SF, Wait JR. Geometrical optical approach for electromagnetic wave propagation in rectangular mine tunnels. Radio Sci. 1974; 9:1147–1158.
5. Didascalou D, Schfer TM, Weinmann F, Wiesbeck W. Ray density normalization for ray-optical wave propagation modeling in arbitrarily shaped tunnels. IEEE Trans Antennas Propag. Sep; 2000 48(9):1316–1325.
6. Hwang Y, Zhang YP, Kouyoumjian RG. Ray-optical prediction of radio-wave propagation characteristics in tunnel environments—Part 1: Theory. IEEE Trans Antennas Propag. Sep; 1998 46(9):1328–1336.
7. Ndoh M, Delisle GY, Le R. A novel approach to propagation prediction in confined and diffracting rough surfaces. Int J Numer Model. 2003; 16:535–555.

Author Manuscript Author Manuscript Author Manuscript Author Manuscript

8. Zhou C, Waynert J. The equivalence of the ray tracing and modal methods for modeling radio propagation in lossy rectangular tunnels. IEEE Antennas Wireless Propag Lett. 2014; 13:615–618.
9. Forooshani AE, Bashir S, Michelson DG, Noghanian S. Asurvey of wireless communications and propagation modeling in underground mines. IEEE Commun Surveys Tuts. Oct-Dec;2013 15(4): 1524–1545.
10. Ramirez L, Hasselmann F, Zhang Y. Channel characteristics in tunnels: FDTD simulations and measurement. J Microw Opt Electromag Appl. 2011; 10:121–130.
11. Ching, GS., Tsuda, K., Kishiki, Y. Analysis of path gain inside tunnels based on FDTD and ray tracing methods. Proc. 2013 Int. Symp. Electromagn. Theory; 2013. p. 644-647.
12. Wu Y, Lin M, Wassell IJ. Modified 2D finite-difference time-domain based tunnel path loss prediction for wireless sensor network applications. J Commun. 2009; 4:214–223.
13. Hadi, MF., Mahmoud, SF. Modeling wireless propagation in a rectangular tunnel with the compact-FDTD method. Proc. 2008 IEEE Radio Wireless Symp; 2008. p. 339-342.
14. Zhou, C., Jacksha, R. Radio propagation analysis in mines and tunnels based on FDTD. Proc. 31st Int. Rev. Progress Appl. Comp. Electromagn; 2015. p. 1-2.
15. Broker, DE., Sidebar, PE., Werner, PL., Werner, DH. A hybrid approach for large-scale optimizations of medium frequency propagation in coal mines. Proc. IEEE Int. Symp. Antennas Propag; 2011. p. 2391-2394.
16. Wagner RL, Jamming S, Chew WC. Monte Carlo simulation of electromagnetic scattering from two-dimensional random rough surfaces. IEEE Trans Antennas Propag. Feb; 1997 45(2):235–245.
17. Waltz C, Sartell K, Carr MA, User BC, Volatize JL. Massively parallel fast multipole method solutions of large electromagnetic scattering problems. IEEE Trans Antennas Propag. Jun; 2007 55(6):1810–1816.
18. Yucel AC, Gomez LJ, Michielssen E. Compression of translation operator tensors in FMM-FFT accelerated SIE solvers via Tucker decomposition. IEEE Antennas Wireless Propag Lett. 2017; 16:2667–2670.
19. Müller, C. Foundations of the Mathematical Theory of Electromagnetic Waves. Vol. 155. New York, NY, USA: Springer; 2013.
20. Rao SM, Wilton DR, Glisson AW. Electromagnetic scattering by surfaces of arbitrary shape. IEEE Trans Antennas Propag. May; 1982 AP-30(3):409–418.
21. Chew, WC., Michielssen, E., Song, JM., Jin, JM. Fast and Efficient Algorithms in Computational Electromagnetics. Norwood, MA, USA: Artech House; 2001.
22. Taboada JM, et al. High scalability FMM-FFT electromagnetic solver for supercomputer systems. IEEE Antennas Propag Mag. Oct; 2009 51(6):20–28.
23. Lathauwer LD, Moor BD, Vandewalle J. A multilinear singular value decomposition. SIAM J Matrix Anal Appl. 2000; 21:1253–1278.
24. Kolda TG, Bader BW. Tensor decompositions and applications. SIAM Rev. 2009; 51:455–500.
25. Freund RW. A transpose-free quasi-minimal residual algorithm for non-hermitian linear systems. SIAM J Sci Comput. 1993; 14:470–482.
26. Zhou C, Waynert J, Plass T, Jacksha R. Attenuation constants of radio waves in lossy-walled rectangular waveguides. Progress Electromagn Res. 2013; 142:75–105.
27. Tsang, L., Kong, JA., Ding, K-H., Ao, CO. Scattering of Electromagnetic Waves, Numerical Simulations. Hoboken, NJ, USA: Wiley; 2004.
28. Bagci H, Yucel AC, Hesthaven JS, Michielssen E. A fast Stroud-based collocation method for statistically characterizing EMI/EMC phenomena on complex platforms. IEEE Trans Electromagn Compat. May; 2009 51(2):301–311.
29. Yucel AC, Bagci H, Michielssen E. An adaptive multi-element probabilistic collocation method for statistical EMC/EMI characterization. IEEE Trans Electromagn Compat. Dec; 2013 55(6):1154–1168.
30. Gomez LJ, Yücel AC, Hernandez-Garcia L, Taylor SF, Michielssen E. Uncertainty quantification in transcranial magnetic stimulation via high-dimensional model representation. IEEE Trans Biomed Eng. Jan; 2015 62(1):361–372. [PubMed: 25203980]

Author Manuscript Author Manuscript Author Manuscript Author Manuscript

31. Yücel AC, Bağcý H, Michielssen E. An ME-PC enhanced HDMR method for efficient statistical analysis of multiconductor transmission line networks. IEEE Trans Compon Packag Manuf Technol. May; 2015 5(5):685–696.
32. Yucel AC, Liu Y, Bagci H, Michielssen E. Statistical characterization of electromagnetic wave propagation in mine environments. IEEE Antennas Wireless Propag Lett. 2013; 12:1602–1605.
33. Velamparambil S, Chew WC. Analysis and performance of a distributed memory multilevel fast multipole algorithm. IEEE Trans Antennas Propag. Aug; 2005 53(8):2719–2727.
34. Taboada JM, Araujo MG, Basteiro FO, Rodriguez JL, Landesa L. MLFMA-FFT parallel algorithm for the solution of extremely large problems in electromagnetics. Proc IEEE. Feb; 2013 101(2): 350–363.

Biographies

Abdulkadir C. Yucel received the B.Sc. degree in electronics engineering (*summa cum laude*) from the Gebze Institute of Technology, Kocaeli, Turkey, in 2005, and the M.Sc. and Ph.D. degrees in electrical engineering from the University of Michigan, Ann Arbor, MI, USA, in 2008 and 2013, respectively.

From August 2006 to April 2013, he was a Graduate Student Research Assistant with the Radiation Laboratory, University of Michigan, where he was a Research Fellow from May 2013 to December 2015. From January 2016 to December 2017, he was a Post-doctoral Researcher with the Research Laboratory of Electronics, Massachusetts Institute of Technology, Cambridge, MA, USA, and the Computational Electromagnetics Group, King Abdullah University of Science and Technology. Since January 2018, he has been an Assistant Professor with the School of Electrical and Electronic Engineering, Nanyang Technological University, Singapore. His research interests include various aspects of computational electromagnetics with emphasis on uncertainty quantification for electromagnetic analysis on complex platforms, electromagnetic compatibility and interference analysis, nature-based design of electromagnetic devices, and integral equation-based frequency and time domain solvers and their accelerators.

Dr. Yucel was the recipient of the Fulbright Fellowship in 2006, the Electrical Engineering and Computer Science Departmental Fellowship of the University of Michigan in 2007, and the IEEE AP-S Student Paper Competition Honorable Mention Award in 2009.

Author Manuscript Author Manuscript Author Manuscript Author Manuscript

Weitian Sheng received the B.S. degree in electronic science and technology from Tongji University, Shanghai, China, in 2013, and the M.S. degree in electrical engineering from the University of Michigan, Ann Arbor, MI, USA, in 2015. He is currently working toward the Ph.D. degree in electrical engineering at the University of Michigan.

Since 2013, he has been a Research Assistant with the Radiation Laboratory, University of Michigan. His current research interests include fast solvers of integral equations, numerical methods in computational electromagnetics, optimization algorithms, and uncertainty quantification methods.

Chenming Zhou (GS'05–M'08) received the Ph.D. degree in electrical engineering from Tennessee Technological University, Cookeville, TN, USA, in 2008.

He is currently a Senior Research Engineer with the National Institute for Occupational Safety and Health (NIOSH), Washington, DC, USA, part of the Centers for Disease Control and Prevention, under the U.S. Department of Health and Human Services. He was the Project Leader and the Principal Investigator for the wireless communications and tracking project at NIOSH. He also was a Government Contract Officer Representative for NIOSH Broad Agency Announcement contracts. Prior to joining NIOSH in August 2012, he was a Research Fellow with the Disney Research Laboratory, Pittsburgh, PA, USA, where he conducted research in RF ranging based on passive RFID tags. Before he started his career in industry for Disney, he was a Project Research Scientist with the Department of Electrical and Computer Engineering, Carnegie Mellon University. He holds 2 U.S. patents in RFID and has authored or co-authored more than 60 papers in peer-reviewed journals or conference proceedings.

Dr. Zhou is currently an Associate Editor for the *IEEE Antennas and Propagation Magazine*.

Author Manuscript Author Manuscript Author Manuscript Author Manuscript

Yang Liu (S'11–M'15) received the B.S. degree in electrical engineering from Shanghai Jiao Tong University, Shanghai, China, in 2010, the M.S. degrees in electrical engineering and mathematics from the University of Michigan, Ann Arbor, MI, USA, in 2013 and 2014, respectively, and the Ph.D. degree in electrical engineering from the University of Michigan, in 2015.

From June 2015 to July 2017, he was a Post-doctoral Fellow with the Radiation Laboratory, University of Michigan. He is currently a Postdoctoral Fellow with the Scalable Solvers Group, Lawrence Berkeley National Laboratory, Berkeley, CA, USA. His research interests include computational electromagnetics, numerical linear algebra, and high-performance computing, with focus on fast iterative and direct solvers for highly oscillatory problems.

Dr. Liu authored the Second Place paper of the Student Paper Competition of the 28th International Review of Progress in Applied Computational Electromagnetics in 2012. He also has coauthored the First Place paper of the Student Paper Competition of the 12th International Workshop on Finite Elements for Microwave Engineering in 2014.

Hakan Bağcý (S'98–M'07–SM'14) received the B.S. degree in electrical and electronics engineering from Bilkent University, Ankara, Turkey, in 2001, and the M.S. and Ph.D. degrees in electrical and computer engineering from the University of Illinois at Urbana–Champaign (UIUC), Champaign, IL, USA, in 2003 and 2007, respectively.

From June 1999 to July 2001, he was an Undergraduate Researcher with the Computational Electromagnetics Group, Bilkent University. From August 2001 to December 2006, he was a Research Assistant with the Center for Computational Electromagnetics and Electromagnetics Laboratory, UIUC. From January 2007 to August 2009, he was a Research Fellow with the Radiation Laboratory, University of Michigan. In August 2009, he joined the Division of Physical Sciences and Engineering, King Abdullah University of Science and Technology, as an Assistant Professor of electrical engineering. His research interests include various aspects of computational electromagnetics with emphasis on time-domain integral equations and their fast marching-on-in-time-based solutions, well-conditioned

Author Manuscript Author Manuscript Author Manuscript Author Manuscript

integral-equation formulations, and development of fast hybrid methods for analyzing statistical EMC/EMI phenomena on complex and fully loaded platforms.

Dr. Bađcý was the recipient of the 2008 International Union of Radio Scientists Young Scientist Award and the 2004–2005 Interdisciplinary Graduate Fellowship from the Computational Science and Engineering Department, UIUC. His paper entitled “Fast and rigorous analysis of EMC/EMI phenomena on electrically large and complex structures loaded with coaxial cables” was one of the three finalists (with honorable mention) for the 2008 Richard B. Schulz Best Transactions Paper Award given by the IEEE Electromagnetic Compatibility Society. He has authored or co-authored nine finalist papers in the Student Paper Competition of the 2005, 2008, 2010, and 2014 IEEE Antennas and Propagation Society International Symposium and the 2013 and 2014 Applied Computational Electromagnetics Society Conference.

Eric Michielssen (F’02) received the M.S. degree in electrical engineering (*summa cum laude*) from the Katholieke Universiteit Leuven, Leuven, Belgium, in 1987, and the Ph.D. degree in electrical engineering from the University of Illinois at Urbana–Champaign (UIUC), Champaign, IL, USA, in 1992.

He joined the faculty of the Department of Electrical and Computer Engineering, UIUC, in 1993, becoming a Full Professor in 2002. In 2005, he joined the University of Michigan (UM), as a Professor of electrical engineering and computer science. Since 2013, he has been the University of Michigan’s Associate Vice President for Advanced Research Computing, and also directs the Michigan Institute for Computational Discovery and Engineering. He has authored or co-authored more than 180 journal papers and book chapters and more than 350 papers in conference proceedings. His research interests include all aspects of theoretical and applied computational electromagnetics. His research interests include the development of fast frequency and time domain integral-equation-based techniques for analyzing electromagnetic phenomena, and the development of robust optimizers for the synthesis of electromagnetic/optical devices.

Dr. Michielssen was a recipient of the Belgian American Educational Foundation Fellowship in 1988 and a Schlumberger Fellowship in 1990. He was also the recipient of a 1994 International Union of Radio Scientists (URSI) Young Scientist Fellowship, a 1995 National Science Foundation CAREER Award, and the 1998 Applied Computational Electromagnetics Society Valued Service Award. In addition, he was named 1999 URSI United States National Committee Henry G. Booker Fellow and was selected as the recipient of the 1999 URSI Koga Gold Medal. He also was the recipient of the UIUC’s 2001 Xerox Award for Faculty Research, appointed 2002 Beckman Fellow of the UIUC Center for

Author Manuscript Author Manuscript Author Manuscript Author Manuscript

Advanced Studies, named 2003 Scholar of the Tel Aviv University Sackler Center for Advanced Studies, and selected as UIUC 2003 University and Sony Scholar. In 2011, he was the recipient of the UM College of Engineering David E. Liddle Research Excellence Award and, in 2014, he was the recipient of the IEEE APS Chen-To-Tai Distinguished Educator Award. He is a member of URSI Commission B.

Appendix I

The entries of the unknown expansion coefficient vector **I** are simply I_n, $n = 1, \ldots, 2N_d + N_p$. The entries of the tested incident field vector **V** are

$$\mathbf{V}_m = \begin{cases} \langle \mathbf{f}_m(\mathbf{r}), \alpha_0 \hat{\mathbf{n}}_d \times \mathbf{E}^i(\mathbf{r}) \rangle_{S_d}, & 1 \le m \le N_d \\ \langle \mathbf{f}_m(\mathbf{r}), \beta_0 \hat{\mathbf{n}}_d \times \mathbf{H}^i(\mathbf{r}) \rangle_{S_d}, & N_d + 1 \le m \le 2N_d \\ \langle \mathbf{f}_m(\mathbf{r}), \alpha_p \hat{\mathbf{t}}_p \cdot \mathbf{E}^i(\mathbf{r}) \rangle_{S_p} + \langle \mathbf{f}_m(\mathbf{r}), \eta_0(1-\alpha_p) \hat{\mathbf{n}}_p \times \mathbf{H}^i(\mathbf{r}) \rangle_{S_p}, & 2N_d + 1 \le m \le N \end{cases} \quad (26)$$

where $\langle \mathbf{a}(\mathbf{r}), \mathbf{b}(\mathbf{r}) \rangle_S = \int_S \mathbf{a}(\mathbf{r}) \cdot \mathbf{b}(\mathbf{r}) d\mathbf{r}$. The entries of the MoM matrix $\bar{\mathbf{Z}}$ are

$$\bar{\mathbf{Z}}_{mn} = 0.5(\alpha_1 - \alpha_0) \langle \mathbf{f}_m(\mathbf{r}), \mathbf{f}_n(\mathbf{r}) \rangle_{S_d} + \langle \hat{\mathbf{n}}_d \times \mathbf{f}_m(\mathbf{r}), (\alpha_1 \mathfrak{R}_1 + \alpha_0 \mathfrak{R}_0)[\mathbf{f}_n(\mathbf{r})] \rangle_{S_d} \; 1 \le m \le N_d, \; 1 \le n \le N_d \quad (27)$$

$$\bar{\mathbf{Z}}_{mn} = -\langle \hat{\mathbf{n}}_d \times \mathbf{f}_m(\mathbf{r}), (\alpha_1 \mathfrak{T}_1 + \alpha_0 \mathfrak{T}_0)[\mathbf{f}_n(\mathbf{r})] \rangle_{S_d} \; 1 \le m \le N_d, \; N_d + 1 \le n \le 2N_d \quad (28)$$

$$\bar{\mathbf{Z}}_{mn} = \langle \hat{\mathbf{n}}_d \times \mathbf{f}_m(\mathbf{r}), \alpha_0 \mathfrak{T}_0[\mathbf{f}_n(\mathbf{r})] \rangle_{S_d} \; 1 \le m \le N_d, \; 2N_d + 1 \le n \le N \quad (29)$$

$$\bar{\mathbf{Z}}_{mn} = -\left\langle \hat{\mathbf{n}}_d \times \mathbf{f}_m(\mathbf{r}), \left(\frac{\beta_1}{\eta_1^2} \mathfrak{T}_1 + \frac{\beta_0}{\eta_0^2} \mathfrak{T}_0 \right) [\mathbf{f}_n(\mathbf{r})] \right\rangle_{S_d} \; N_d + 1 \le m \le 2N_d, \; 1 \le n \le N_d \quad (30)$$

Author Manuscript Author Manuscript Author Manuscript Author Manuscript

$$\overline{\mathbf{Z}}_{mn} = 0.5(\beta_0 - \beta_1)\langle \mathbf{f}_m(\mathbf{r}), \mathbf{f}_n(\mathbf{r})\rangle_{S_d} - \langle \hat{\mathbf{n}}_d \times \mathbf{f}_m(\mathbf{r}), (\beta_1 \mathfrak{R}_1 + \beta_0 \mathfrak{R}_0)[\mathbf{f}_n(\mathbf{r})]\rangle_{S_d} N_d + 1 \le m \le 2N_d,\ N_d + 1 \le n \le 2N_d$$

(31)

$$\overline{\mathbf{Z}}_{mn} = \langle \hat{\mathbf{n}}_d \times \mathbf{f}_m(\mathbf{r}), \beta_0 \mathfrak{R}_0[\mathbf{f}_n(\mathbf{r})]\rangle_{S_d} N_d + 1 \le m \le 2N_d,\ 2N_d + 1 \le n \le N \quad (32)$$

$$\overline{\mathbf{Z}}_{mn} = \langle \mathbf{f}_m(\mathbf{r}), -\hat{\mathbf{t}}_p \cdot \alpha_p \mathfrak{R}_0[\mathbf{f}_n(\mathbf{r})]\rangle_{S_p} - \langle \hat{\mathbf{n}}_p \times \mathbf{f}_m(r), (1-\alpha_p)/\eta_0 \mathfrak{T}_0[\mathbf{f}_n(\mathbf{r})]\rangle_{S_p} 2N_d + 1 \le m \le N,\ 1 \le n \le N_d$$

(33)

$$\overline{\mathbf{Z}}_{mn} = \langle \mathbf{f}_m(\mathbf{r}), \hat{\mathbf{t}}_p \cdot \alpha_p \mathfrak{T}_0[\mathbf{f}_n(\mathbf{r})]\rangle_{S_p} - \langle \hat{\mathbf{n}}_p \times \mathbf{f}_m(\mathbf{r}), \eta_0(1-\alpha_p)\mathfrak{R}_0[\mathbf{f}_n(\mathbf{r})]\rangle_{S_p} 2N_d + 1 \le m \le N,\ N_d + 1 \le n \le 2N_d$$

(34)

$$\overline{\mathbf{Z}}_{mn} = \langle \mathbf{f}_m(\mathbf{r}), -\hat{\mathbf{t}}_p \cdot \alpha_p \mathfrak{T}_0[\mathbf{f}_n(\mathbf{r})]\rangle_{S_p} + \eta_0(1-\alpha_p) \left(0.5\langle \mathbf{f}_m(\mathbf{r}), \mathbf{f}_n(\mathbf{r})\rangle_{S_p} + \langle \hat{\mathbf{n}}_p \times \mathbf{f}_m(\mathbf{r}), \mathfrak{R}_0[\mathbf{f}_n(\mathbf{r})]\rangle_{S_p}\right) \quad (35)$$
$$2N_d + 1 \le m \le N,\ 2N_d + 1 \le n \le N.$$

Appendix II

The parallelization strategy used in this paper is built on the hybrid spatial/angular partitioning approach that was originally developed for multilevel FMM[33]. This strategy achieves uniform memory computational load distribution (among N_p processors) during the setup stage as follows: Each processor is in charge of computing and storing the matrices

Author Manuscript Author Manuscript Author Manuscript Author Manuscript

that hold near-field interactions and basis functions' far-fields and receiving patterns for N_g/N_p groups (spatial partitioning), where N_g stands for the total number of groups enclosing the basis functions. In addition, each processor is responsible for computing and storing the FFT'ed translation operator tensors for $\sum_{a=0}^{1}(K_a+1)(2K_a+1)/N_p$ plane wave directions (angular partitioning). No communication among processors is required at this stage. During the matrix–vector multiplication stage, the uniform computational load partitioning is achieved by the following steps, depicted for an example structure in Fig. 8.

Step 1: Each processor computes the outgoing far-field and receiving patterns of the groups (along all directions) that it is responsible for. Then it sends a set of directions of each group's far-fields to the processor that is in charge of that set of directions. At the same time, it receives all remaining groups' far-fields along a set of directions that it is responsible for. This process can be better explained on the example structure in Fig. 8: Each pair of concentric circles represents one group's far-field (or receiving) patterns; outer and inner circles represent the far-field (or receiving) patterns computed for the medium 1 and medium 0 (air), respectively. The angular dimension of each circle concerns the angular samples (or directions) of the far-field (or receiving) pattern. The number printed inside/near (and color of) the concentric circles/arcs indicates the ID of the processor in charge of the data. For the example structure, each processor computes three groups' far-field patterns along all directions [via (15)] and keeps a quarter of this data (as $N_p = 4$) that is pertinent to directions the processor is responsible for. It sends the remaining portion of this data to the other processors that are responsible for the remaining directions. At the same time, it receives the data from other processors pertinent to remaining groups' far-fields along a set of directions that it is responsible for. The send and receive operations are performed using nonblocking MPI commands.

Step 2: Each processor has all groups' outgoing far-field patterns and FFT'ed translation operator tensors for a set of directions that it is responsible for (shown by arcs in Fig. 8). Using this data, each processor performs the translation operation (via (17)) and obtains incoming plane wave spectra for each direction that it is in charge of. Then it sends each group's incoming wave spectrum along a set of directions to the processor that is in charge of that group. At the same time, it receives the incoming wave spectrum along remaining directions from the other processors for each group that the processor is responsible for. Again, send and receive operations are performed using nonblocking MPI commands.

Step 3: Each processor has the incoming plane wave spectra of the groups (along all directions) that it is responsible for. Using each group's incoming plane wave spectrum and receiving pattern of the basis function that sits in that group, it computes the far-field contribution to the matrix–vector multiplication pertinent to mth basis function.

As each processor computes and stores near-field interaction matrices of each group that it is in charge of, it also locally computes the near-field contribution to the matrix–vector multiplication pertinent to mth basis function that sits in that group. At the end of each matrix–vector multiplication, each processor sums the near- and far-field contributions

Author Manuscript Author Manuscript Author Manuscript Author Manuscript

pertinent to all basis functions that sit in groups that the processor is responsible for. Then it writes the results to the pertinent entries of a vector with dimension N, which is distributed to all processors by all-to-all communication (MPI_Allreduce). It should be mentioned here that the parallelization strategy used in this paper is similar to the one described in [34]. However, there are several differences in their implementation. The parallelization scheme described above makes use of nonblocking send/receive communications as opposed to all-to-all communications. Furthermore, the strategy in [34] uses each core of the processor to compute the 3-D FFTs in (17) serially for the directions assigned to it at the translation stage while in this paper, the 3-D FFTs for each direction are computed using all cores of each processor in parallel via an OpenMP-FFT library, as explained in [18].

Author Manuscript Author Manuscript Author Manuscript Author Manuscript

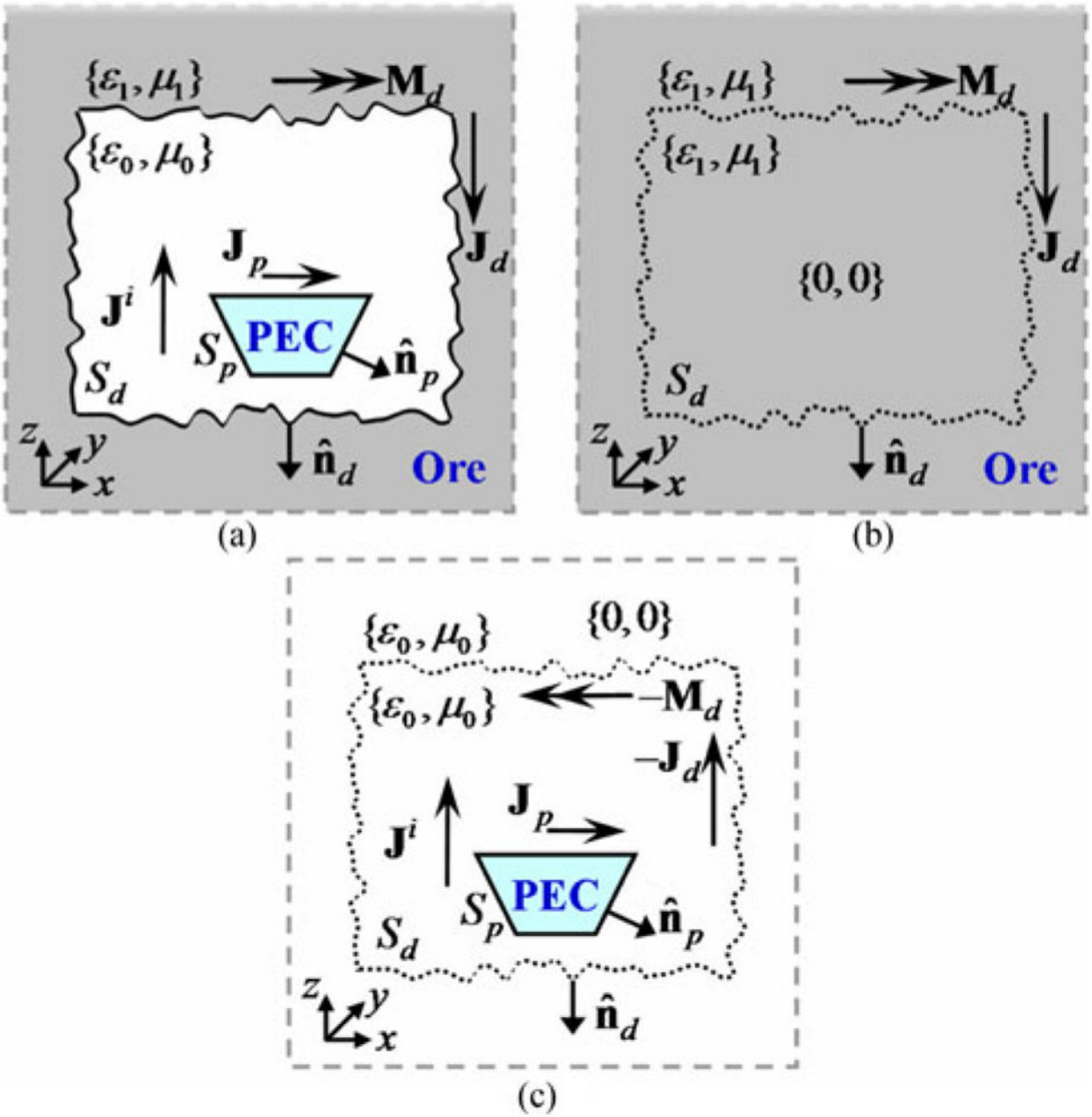

Fig. 1.

Generic tunnel geometry for Muller-combined field SIE formulation. (a) Original problem. (b) Equivalent exterior problem. (c) Equivalent interior problem.

Author Manuscript Author Manuscript Author Manuscript Author Manuscript

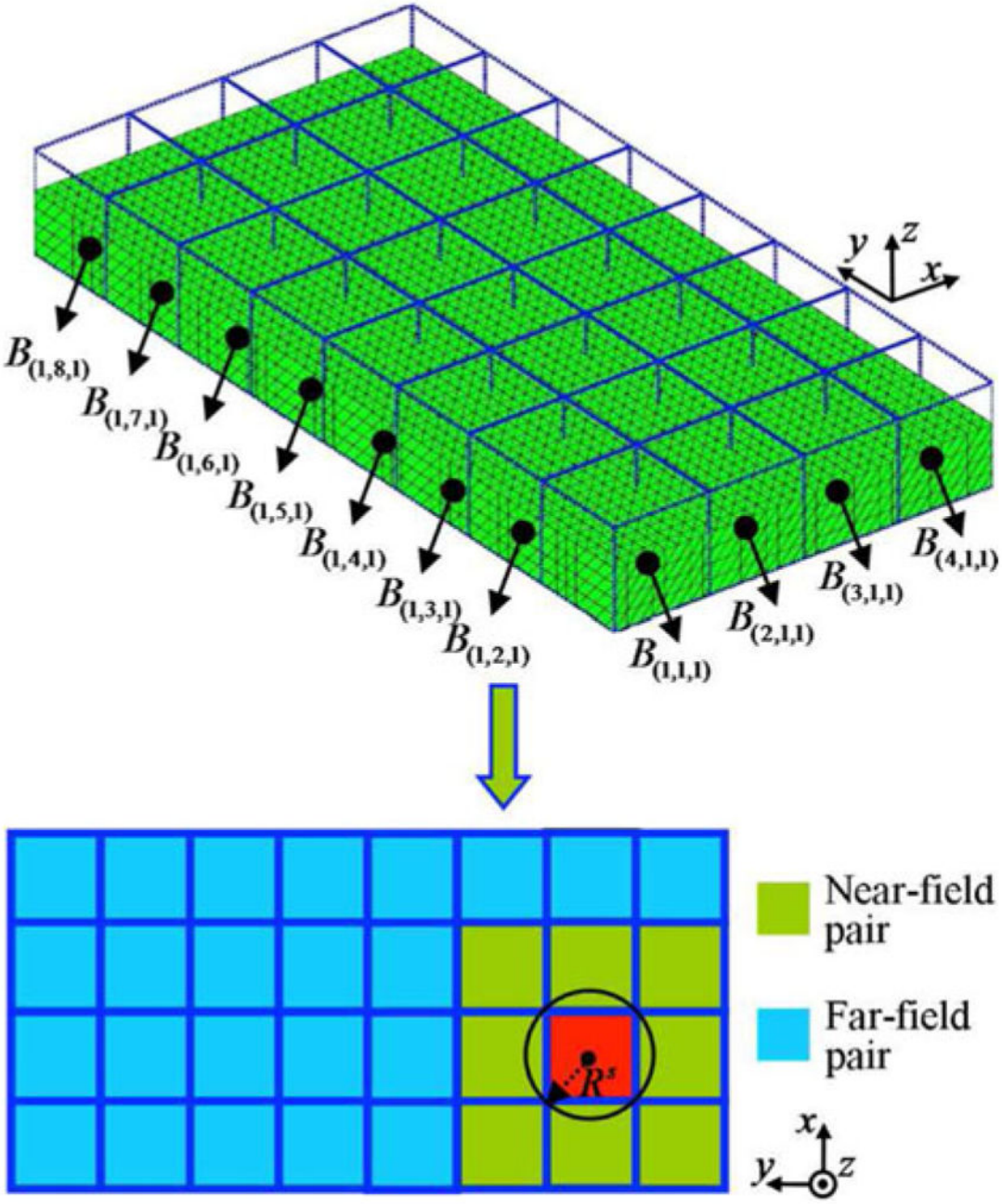

Fig. 2.

Partitioning a fictitious box enclosing the mesh of an example structure into small boxes and tabulating near/far-field pairs of a selected group $B_{(2,2,1)}$ in an FMM-FFT scheme.

Author Manuscript Author Manuscript Author Manuscript Author Manuscript

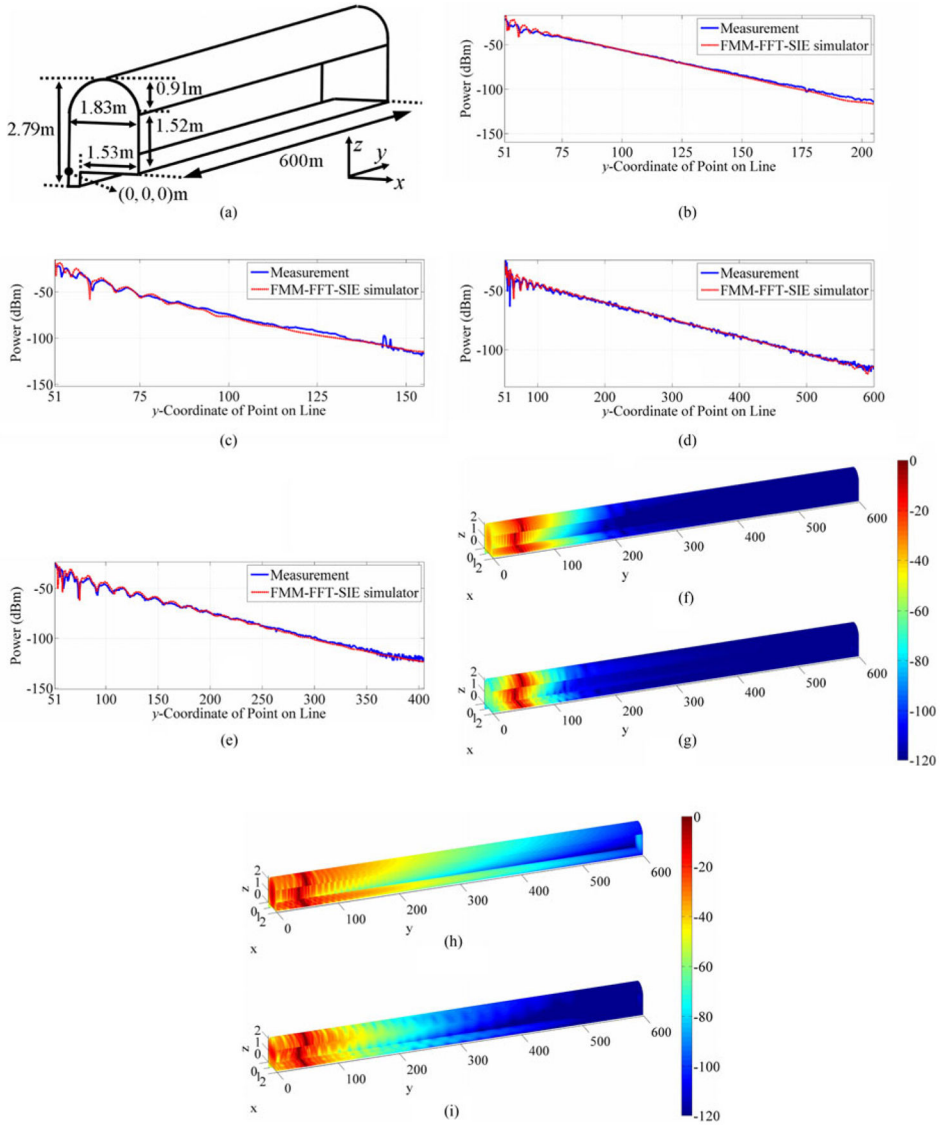

Fig. 3.

(a) Geometry of an empty 600 m-long arched tunnel (the lateral wall is removed for illustration). The power values on receiver points computed by the proposed FMM-FFT-SIE simulator and obtained by measurements at 455 MHz for (b) vertical and (c) horizontal polarizations and at 915 MHz for (d) vertical and (e) horizontal polarizations. Electric current density on tunnel walls computed by the proposed simulator at 455 MHz for (f) vertical and (g) horizontal polarizations and at 915 MHz for (h) vertical and (i) horizontal polarizations (in dB scale).

Author Manuscript Author Manuscript Author Manuscript Author Manuscript

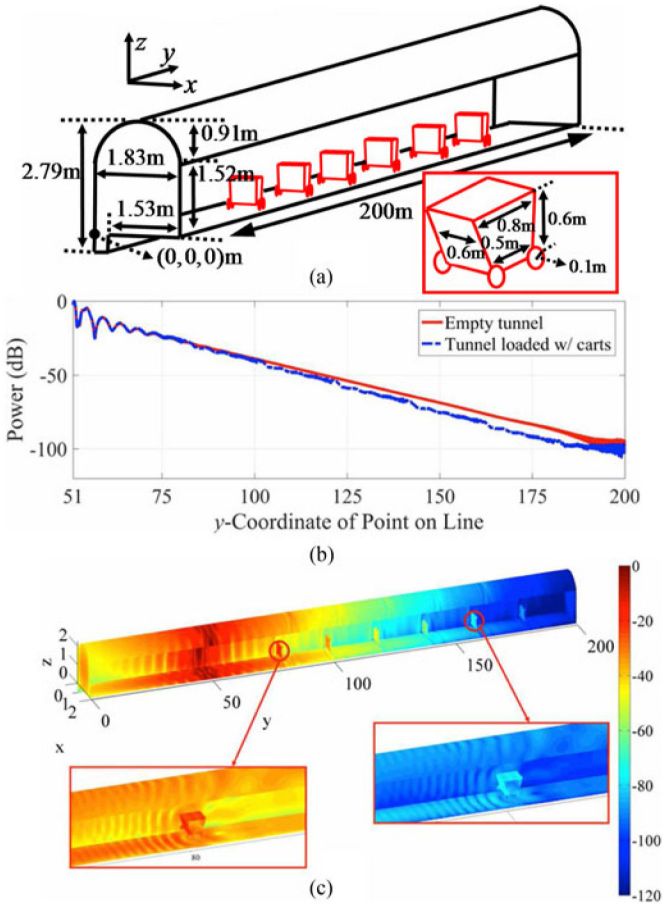

Fig. 4.

(a) Geometry of a 200-m-long arched tunnel loaded with six PEC mine carts (the lateral wall is removed for illustration). (b) Power values on receiver points in empty and loaded tunnels computed by the proposed FMM-FFT-SIE simulator. (c) Electric current density on tunnel walls and mine carts computed by the proposed simulator (in dB scale).

Author Manuscript Author Manuscript Author Manuscript Author Manuscript

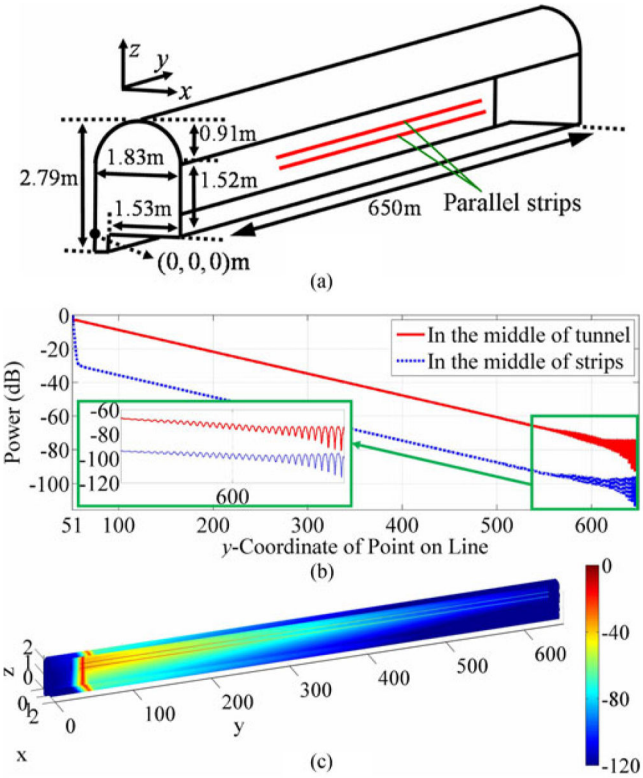

Fig. 5.

(a) Geometry of a 650-m-long arched tunnel loaded with two parallel PEC strips (the lateral wall is removed for illustration). (b) Power values at receiver points on a line in the middle of the strips and on a line in the middle of the tunnel computed by the proposed simulator. (c) Electric current density on tunnel walls and conductor strips computed by the proposed simulator (in dB scale) (the half of the tunnel is removed to clearly show the currents around the strips).

Author Manuscript Author Manuscript Author Manuscript Author Manuscript

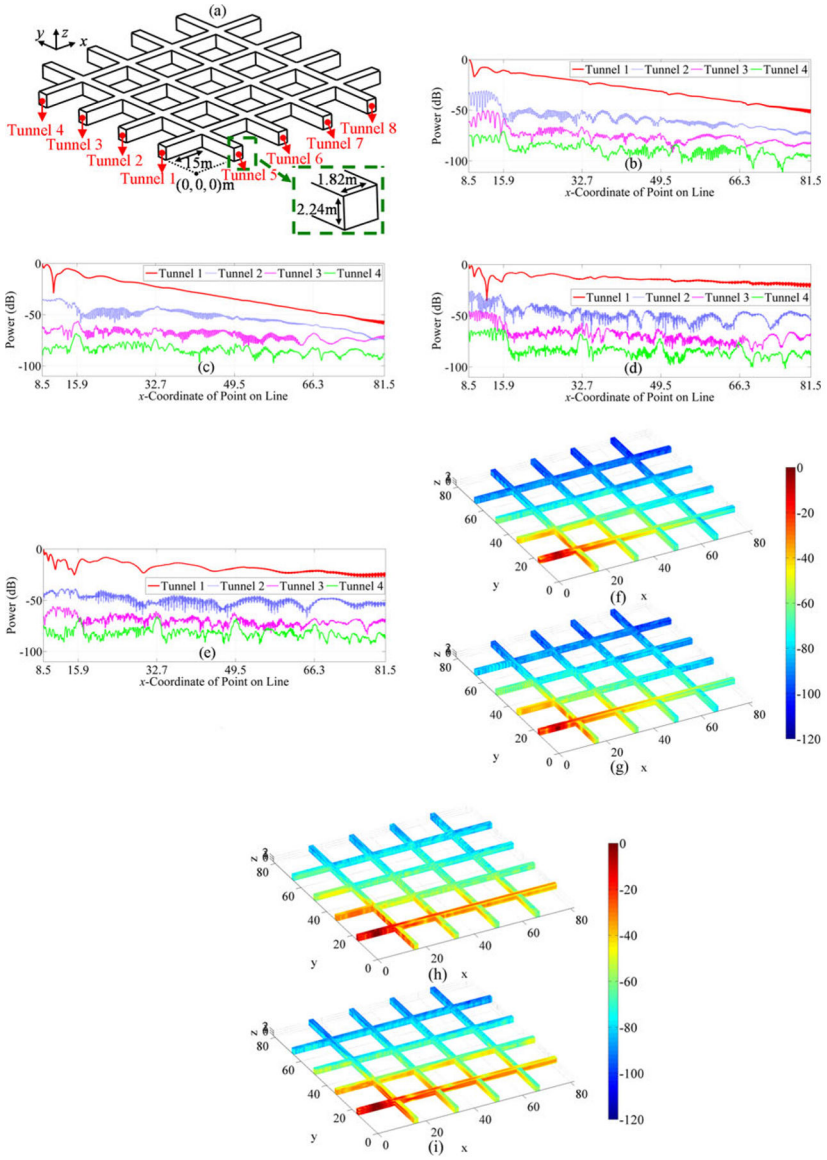

Fig. 6.

(a) Geometry of a mine gallery formed by eight tunnels. (b) Power values at receiver points on lines inside tunnel 1, 2, 3, and 4 computed by the proposed FMM-FFT-SIE simulator at 455 MHz for (b) vertical and (c) horizontal polarizations and at 915 MHz for (d) vertical and (e) horizontal polarizations. Electric current density on tunnel walls computed by the proposed simulator at 455 MHz for (f) vertical and (g) horizontal polarizations and at 915 MHz for (h) vertical and (i) horizontal polarizations (in dB scale).

Author Manuscript Author Manuscript Author Manuscript Author Manuscript

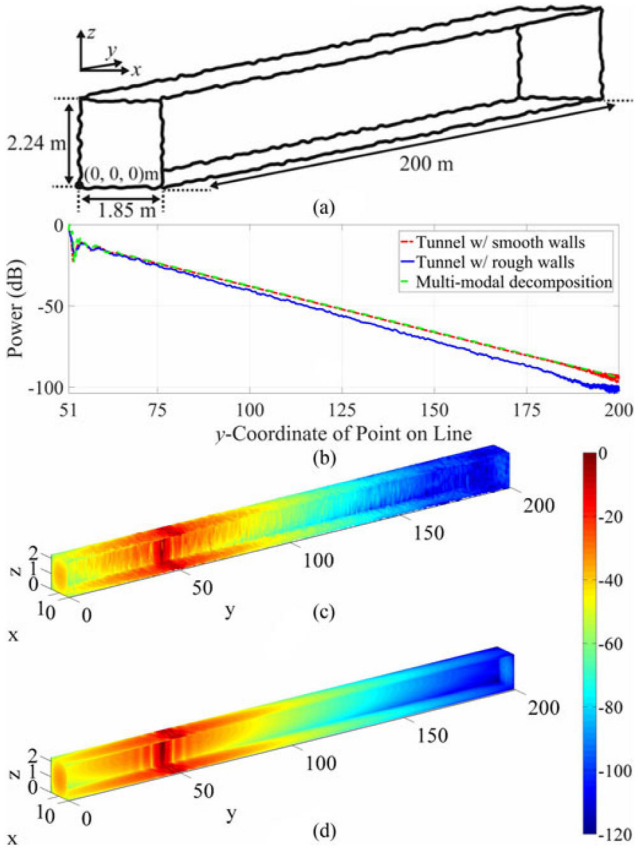

Fig. 7.

(a) Geometry of a 200-m-long rectangular tunnel with rough walls. (b) Power values at receiver points on a line in the middle of the tunnel computed by the proposed simulator for the tunnel with smooth and rough walls and by the multi-modal decomposition for the tunnel with smooth walls. Electric current density on (c) rough walls and (d) smooth walls of the rectangular tunnel computed by the proposed simulator (in dB scale).

Author Manuscript Author Manuscript Author Manuscript Author Manuscript

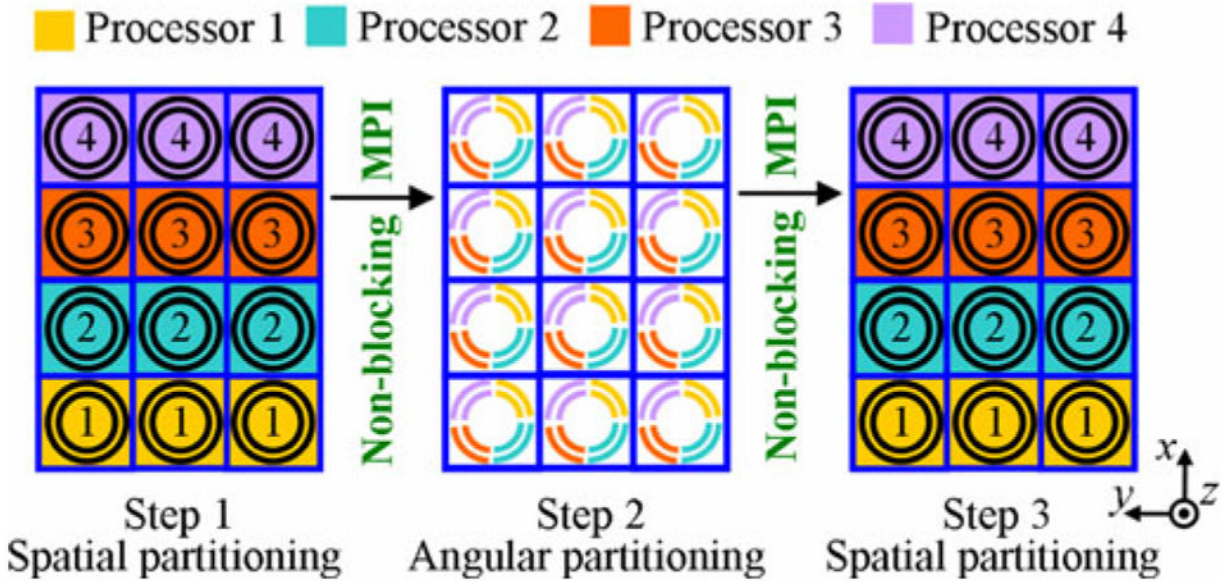

Fig. 8.

Parallelization strategy in the FMM-FFT scheme for matrix-vector multiplication stage: partitioning of groups and plane wave directions among $N_p = 4$ processors for an example structure composed of 4 and 3 groups along x and y directions.

Author Manuscript Author Manuscript Author Manuscript Author Manuscript

TABLE I

Specifications of Simulations Performed by FMM-FFT-SIE Solver for Each Numerical Example

Numerical Example	Frequency (MHz)	Polarization	Number of processors used for simulation	Average memory required for each processor (GB)		Total simulation time (hours (h)/minutes (min))
				Without Compression	With Compression	
Empty arched tunnel (Section III-A.1)	455	Vertical	32	28.40	14.62	5 h/17 min
		Horizontal				5 h/20 min
	915	Vertical	45	64.91	36.45	29 h/54 min
		Horizontal				28 h/49 min
Arched tunnel loaded with carts (Section III-A.2)	455	Vertical	16	20.09	10.58	4 h/27 min
Arched tunnel loaded with strips (Section III-A.3)	50	Vertical	32	2.28	-	9 h/22 min
Mine gallery (Section III-B)	455	Vertical	32	21.05	10.60	4 h/52 min
		Horizontal				4 h/38 min
	915	Vertical	45	46.27	28.89	23 h/52 min
		Horizontal				22 h/45 min
Rectangular tunnel with rough walls (Section III-C)	455	Vertical	32	30.04	12.73	6 h/22 min
Rectangular tunnel with smooth walls (Section III-C)	455	Vertical	32	28.45	12.28	6 h/45 min

IEEE J Multiscale Multiphys Comput Tech. Author manuscript; available in PMC 2018 May 01.